Fluorescence Optical Tomography

Jenghwa Chang[1], Randall L. Barbour[1,2], Harry Graber[2], Raphael Aronson[3]

Department of Pathology[1] and Department of Physiology and Biophysics[2]
SUNY Health Science Center at Brooklyn; Bioimaging Sciences Corporation[3]

Abstract

Two one-speed radiation transport equations coupled by a dynamic equation for the distribution of fluorophore electronic states were used to model the migration of excitation photons and emitted fluorescent photons. The conditions for producing appreciable levels of the fluorophore in the excited state were studied, and we concluded that under the conditions applicable to tissue imaging, minimal saturation occurs. This simplified the derivation of the frequency response for a time-harmonic excitation source and of the imaging operator. Several factors known to influence the fluorescence response have been examined. Among these are the concentration, mean lifetime and quantum yield of the fluorophore, and the modulation frequency of the excitatory source. The fluorescence source strength was calculated as a function of the mean lifetime and modulation frequency. Results showed that optimal sensitivity is achieved by fluorophores having short lifetimes and excitation modulation frequencies in the 50-200 MHz range. The dependence of demodulation of the fluorescent signal on the above factors was also examined. Results showed that demodulation increases at longer lifetimes and higher modulation frequencies.

In additional studies, tomographic imaging operators based on transport theory were derived for imaging fluorophore concentrations embedded in a highly scattering medium. Experimental data were collected by irradiating a cylindrical phantom containing one or two fluorophore–filled balloons with CW laser light. The reconstruction results show that good quality images can be obtained, with embedded objects accurately located.

1. Introduction

Radiolabeled and fluorescent tagged biomolecules have been successfully used in a range of biomedical research studies for many years. In practical medical imaging, *e.g.*, nuclear medicine and SPECT and PET imaging, however, only radioisotopes are widely used to provide useful anatomic and physiological information. Use of fluorescent probes in clinical studies has been limited mostly to *in vitro* examination of stained tissue slices. In the clinical laboratory, fluorescent probes have successfully replaced use of radioisotopes in many applications. The possibility of employing fluorescent probes as substitutes for radioisotopes for thick tissue imaging is complicated by the intense scattering of optical photons. One result of this is that many efficient algorithms developed for x-ray tomography, *e.g.*, Fourier slice theory [1,2] are not applicable to the optical imaging problem.

The fluorescence phenomenon involves the emission of photons from singlet excited states [3]. There basically is a three-step process: generation of the excited states (S_1, S_2, S_3, ...) by absorption of a photon, loss of energy by internal conversion and return to the lowest vibration level of S_1, and return to the ground state by radiative emission. Both radiative and nonradiative processes serve to depopulate the excited state. For a particular fluorophore and illumination condition, several useful quantities can be measured. These are the mean and intrinsic lifetimes, and the quantum yield. The mean lifetime is defined as the average time a molecule spends in the excited state, and is equal to the inverse of the sum of the radiative and nonradiative decay constants. The intrinsic lifetime is the lifetime when nonradiative processes are absent and is equal to the inverse of the radiative decay constant. The ratio of the number of emitted photons to the number of absorbed photons is called the quantum yield and is equal to the ratio of the mean to intrinsic lifetimes [3].

Optical imaging of tissues using tomographic illumination and detection schemes has attracted significant interest for the past few years [4,5]. In most cases, perturbation methods embodying either the Born or Rytov approximations are used for analysis of time–resolved, time–harmonic, or continuous–wave (CW) measurements. This approach analyzes the difference between measurements obtained at the boundary of reference and test media and uses this information to reconstruct cross-sectional images of the differences between the media. The difference signal is usually very small and is sensitive to noise. Use of fluorescent light for optical imaging of tissues, on the other hand, has

several important advantages. First is the fact that fluorescence measurements are intrinsically much more sensitive than absorption-scattering measurements. This is because in the absence of the fluorophore, which itself is the perturbing agent, the reference intensity is zero. Other advantages include the fact that the physical properties of a fluorophore can be sensitive to its immediate chemical environment. Thus, a fluorescence tomography method has properties similar to MRI but at a sensitivity level orders of magnitude greater. In addition, by linking the fluorophore to a targeting biomolecule (e.g., monoclonal antibody) the fluorescence tomography method becomes similar to radioscintillographic imaging methods but without the need for exposure to ionizing radiation.

In this paper, we study the excitation and emission in fluorescence phenomenon using two coupled one-speed transport equations. The governing equation describing the fractional excited state fluorophore concentration was also studied and nonsaturation conditions and allowable excitation intensities were determined to simplify the problem. Sensitivity of fluorescence emission to changes in the mean lifetime and modulation frequency were studied and the demodulation caused by the fluorophore was explored. Further, we derived an imaging operator based on transport theory. The final form of this operator is a system of linear equations which can be easily solved by iterative methods. Monte Carlo simulations were performed to calculate this operator. Experimental data were collected using a CT-type scanning laser system. Image reconstructions were performed using projection onto convex sets (POCS) [6], conjugate gradient descent (CGD) [7], and simultaneous algebraic reconstruction technique (SART) [1] methods.

2. Theory

Governing Equations

Light propagation in a material can be described by the time–dependent radiative transfer equation (RTE) [8],

$$\frac{1}{c}\frac{\partial \phi}{\partial t} + \Omega \cdot \nabla \phi + \mu_T \phi = s + \int_0^\infty \int_{4\pi} \mu_S(\mathbf{r}, \Omega' \cdot \Omega, E' \to E)\phi' \, d\Omega' dE' , \tag{1}$$

where c is the speed of light, E is the energy of the photon, $d\Omega$ is the differential solid angle [sr], $\phi = \phi(\mathbf{r}, \Omega, E, t)$ and $\phi' = \phi(\mathbf{r}', \Omega', E', t)$ are angular intensities [cm^{-2} s^{-1} sr^{-1}], $s = s(\mathbf{r}, \Omega, E, t)$ is the angular source strength [cm^{-3} s^{-1} sr^{-1}], $\mu_S(\mathbf{r}, \Omega' \cdot \Omega, E' \to E)$ is the macroscopic differential scattering cross section [cm^{-1} sr^{-1}], and $\mu_T = \mu_T(\mathbf{r}, E)$ is the macroscopic total cross section [cm^{-1}]. In this study, we assume that the excitation and emitted light are monoenergetic with energies E_1 and E_2, respectively. Then (1) reduces to two coupled equations. For the excitation intensity,

$$\frac{1}{c}\frac{\partial \phi_1}{\partial t} + \Omega \cdot \nabla \phi_1 + \left(\mu_{T,1} + \mu_{T,1\to2}\right)\phi_1 = s_1 + \int_{4\pi} \mu_{S,1}(\Omega' \cdot \Omega)\phi_1' \, d\Omega' , \tag{2}$$

where $\mu_{T,1}$ is the total cross section of the reference medium for E_1, and $\mu_{T,1\to2}$ is the change in total cross section after the fluorophore is added. That is,

$$\mu_{T,1\to2} = N_g \Sigma_{T,1\to2} , \tag{3}$$

where $\Sigma_{T,1\to2}$ is the microscopic total cross section [cm^2] of the fluorophore and N_g is the concentration of the fluorophore in the ground state. This, in turn, is governed by the following equation:

$$\frac{dN_g}{dt} = -\Sigma_{T,1\to2}\overline{\phi}_1 N_g + \frac{1}{\tau}(N_0 - N_g), \tag{4}$$

or

$$\frac{dN_s}{dt} = -\frac{1}{\tau}N_s + \Sigma_{T,1\to2}\overline{\phi}_1(N_0 - N_s),\tag{5}$$

where N_0 is the total fluorophore concentration (ground and excited electronic states), $N_s = N_0 - N_g$ is the concentration of the excited fluorophore, $\overline{\phi}_1 = \overline{\phi}_1(\mathbf{r},t) = \int_{4\pi}\phi_1 d\Omega$ is the intensity [cm^{-2} s^{-1}] of the excitation light and τ is the mean lifetime of the fluorescent probe's excited state. The following is a theoretical treatment of only the excitation and fluorescence intensities and does not consider fluorescence polarization or other anisotropic phenomena.

In an ideal case, where only one fluorophore species is present in a homogeneous environment, the impulse response of (5) is a monoexponential decay. However, multi-exponential decay can be observed for a mixture of fluorophores with different mean lifetimes, or for a single fluorophore species in a heterogeneous environment. In this study, we consider the cases of a single fluorophore in a heterogeneous environment and of a mixture of two or more fluorophore species whose emissions can be excited or detected *separately*. The RTE for the fluorescence intensity is:

$$\frac{1}{c}\frac{\partial\phi_2}{\partial t} + \Omega\cdot\nabla\phi_2 + \mu_{T,2}\phi_2 = \frac{\gamma}{4\pi\tau}N_s + \int_{4\pi}\mu_{S,2}(\Omega'\cdot\Omega)\phi_2' d\Omega' = s_2 + \int_{4\pi}\mu_{S,2}(\Omega'\cdot\Omega)\phi_2' d\Omega',\tag{6}$$

where $\gamma = \tau/\tau_0$ is the quantum efficiency and τ_0 is the intrinsic lifetime of the fluorescent probe's excited state. Let R be the reading of a given detector for the emitted intensity, and $r = r_2(\mathbf{r},\Omega,E,t)$ be the detector sensitivity function. Then

$$R = \int_V\int_{4\pi}r_2 \otimes\left(\int_{V'}\int_{4\pi}s_2' \otimes G_2(\mathbf{r},\Omega;\mathbf{r}',\Omega';t)d\Omega'd^3r'\right)d\Omega d^3r$$

$$= \int_{V'}\int_{4\pi}s_2' \otimes\left(\int_V\int_{4\pi}r_2 \otimes G_2(\mathbf{r}',-\Omega';\mathbf{r},-\Omega;t)d\Omega d^3r\right)d\Omega'd^3r'$$

$$= \int_V\int_{4\pi}\frac{\gamma}{4\pi\tau}N_s \otimes\phi_2^+ d\Omega d^3r = \int_V\frac{\gamma}{4\pi\tau}N_s \otimes\overline{\phi}_2^+ d^3r,\tag{7}$$

where the $\otimes$ symbol denotes a convolution in time, and

$G_2(\mathbf{r},\Omega;\mathbf{r}',\Omega';t) =$ Green's function at $\mathbf{r}$ and direction Ω, with source located at $\mathbf{r}'$ and direction Ω',

$$\phi_2^+ = \int_{V'}\int_{4\pi}r_2' \otimes G_2(\mathbf{r},-\Omega;\mathbf{r}',-\Omega';t)d\Omega'd^3r',$$

$$\overline{\phi}_2^+ = \int_{4\pi}\phi_2^+ d\Omega.$$

Frequency Domain Response

Equation (7) describes the expected fluorescence response of a time–resolved detector to a time–resolved source. Experimentally, it is more convenient to consider time–harmonic or time–independent measurements. Inspection of equations (4) and (5) shows that the temporal derivative of the ground state fluorophore concentration is a function of the product of the concentration itself and the excitation field intensity. Because of this, a time–harmonic excitation will produce an *an*harmonic periodic signal containing the fundamental frequency and all its overtones. This situation is problematic because subsequent analysis to infer properties of an unknown medium would require consideration of all these frequencies. This occurs when the population of the excited state becomes appreciable, *i.e.*, when the fluorophore is partially saturated. When the saturation level is not significant, *i.e.*, $N_g \approx N_0$, the contribution of the higher order harmonics can be safely ignored, permitting the following simplifications. By replacing N_g in the first term on the right

side of equation (4), and $N_0 - N_s$ in the second term of the right hand side of equation (5), both with N_0, and then Fourier transforming equations (4) and (5), we obtain

$$\widetilde{N}_g = \frac{2\pi N_0 \delta(\omega) - \tau \Sigma_{T,1\to2} N_0 \widetilde{\widetilde{\phi}}_1}{1 + j\omega\tau},$$ (8)

$$\widetilde{N}_s = \frac{\tau \Sigma_{T,1\to2} N_0 \widetilde{\widetilde{\phi}}_1}{1 + j\omega\tau}.$$ (9)

The associated detector response is

$$\widetilde{R} = \int_V \frac{\gamma \Sigma_{T,1\to2} N_0 e^{-j\tan^{-1}\omega\tau}}{4\pi\sqrt{1 + \omega^2\tau^2}} \widetilde{\widetilde{\phi}}_1 \widetilde{\widetilde{\phi}}_2^+ d^3r,$$ (10)

which defines a time–harmonic emissive field.

The Inverse Problem

The goal of the inverse problem is to solve equation (10) for $\mu_{T,1\to2}$, γ, and τ under different source and detection conditions. This requires two reconstruction steps. Each step involves solving a system of linear equations to calculate the optical coefficients. This system, $\mathbf{W}\mu = \mathbf{R}$, is the discretized form of an integral equation, where $\mathbf{W}$ is the so–called weight matrix, μ is the vector of optical coefficients to be solved, and $\mathbf{R}$ is the vector of detector readings. In the first step, we solve for the background absorption and scattering coefficients, μ_a and μ_s, of the medium for the excitation and the emission photons separately. This can be achieved using previously developed techniques for imaging scattering and absorption coefficients [9,10]. The second step is to reconstruct $\mu_{T,1\to2}$, γ, and τ using estimates of $\widetilde{\widetilde{\phi}}_1$ and $\widetilde{\widetilde{\phi}}_2^+$ calculated from Monte Carlo simulations or other numerical methods (*e.g.*, finite element method, discrete ordinates method) using the coefficients obtained from the first step. The following are two proposed methods for this second step.

(A) DC source

If we use DC sources, then equation (10) becomes

$$\widetilde{R} = \int_V \frac{\Sigma_{T,1\to2} \widetilde{\widetilde{\phi}}_1 \widetilde{\widetilde{\phi}}_2^+}{4\pi} (\gamma N_0) d^3r = \int_V w(\gamma N_0) d^3r,$$ (11)

where $w \equiv w_{\mathrm{DC}} = \dfrac{\Sigma_{T,1\to2} \widetilde{\widetilde{\phi}}_1 \widetilde{\widetilde{\phi}}_2^+}{4\pi}$ is the weight function. If $\Sigma_{T,1\to2}$ is known and $\widetilde{\widetilde{\phi}}_1$ and $\widetilde{\widetilde{\phi}}_2^+$ can be precalculated assuming that fluorophore is not present, then the unknown quantity γN_0 can be computed by solving a linear system obtained by discretizing (11). Here, only the product of quantum efficiency and fluorophore concentration is found, and they can not be directly separated.

(B) AC source

If modulated sources are used and γN_0 is solved for by analyzing the DC component of the response as described above, then equation (10) becomes

$$\widetilde{R} = \int_V \frac{1}{1+j\omega\tau} \frac{\gamma\Sigma_{T,1\to2}N_0\widetilde{\overline{\phi}}_1\widetilde{\overline{\phi}}_2^+}{4\pi} d^3r = \int_V w\frac{1-j\omega\tau}{1+\omega^2\tau^2}d^3r,$$ (12)

where $w \equiv w_{AC} = \dfrac{\gamma\Sigma_{T,1\to2}N_0\widetilde{\overline{\phi}}_1\widetilde{\overline{\phi}}_2^+}{4\pi} = \gamma N_0 w_{DC}$. Equation (12) can be discretized, and the real and imaginary parts of the

detector readings give rise to two distinct systems of linear equations, from which $1/(1+\omega^2\tau^2)$ and $-\omega\tau/(1+\omega^2\tau^2)$ can be reconstructed. Because ω is known, τ can also be deduced.

3. Saturation Condition for a Modulated Waveform

If the excitation is a modulated waveform, with $\widetilde{\overline{\phi}}_1 = \phi_1^0\left[2\pi\delta(\omega) + \pi\eta\delta(\omega - \omega_0) + \pi\eta\delta(\omega + \omega_0)\right]$, where ϕ_1^0 is the DC

amplitude, η is the modulation, and ω_0 is the modulation frequency, then

$$\widetilde{N}_g(0) = 2\pi N_0\left(1 - \tau\Sigma_{T,1\to2}\phi_1^0\right)\delta(\omega)$$ (13)

for DC, and

$$\widetilde{N}_g(\omega_0) = \frac{-\eta\pi\tau\Sigma_{T,1\to2}\phi_1^0}{1+j\omega_0\tau}\delta(\omega - \omega_0)N_0$$ (14)

for AC. Now, $\widetilde{N}_0 = 2\pi N_0\delta(\omega)$. In deriving equations (8) – (10), it was assumed that fluorophore saturation is

negligible, $i.e.$, $N_g \approx N_0$. We should also expect that $\widetilde{N}_g \approx \widetilde{N}_0$, in which case $\widetilde{N}_g(0) \approx 2\pi N_0\delta(\omega)$ and $\widetilde{N}_g(\omega_0) \approx 0$.

These approximations are valid if the following conditions are met:

$$1 - \tau\Sigma_{T,1\to2}\phi_1^0 \approx 1, \qquad \left|\frac{\eta\pi\tau\Sigma_{T,1\to2}\phi_1^0}{1+j\omega_0\tau}\right| \ll 1,$$

or

$$\tau\Sigma_{T,1\to2}\phi_1^0 \ll 1, \qquad \frac{\eta\pi\tau\Sigma_{T,1\to2}\phi_1^0}{\sqrt{1+\omega_0^2\tau^2}} \ll 1$$

As $\eta \leq 1$ and $\left(1 + \omega_0^2\tau^2\right)^{-1/2} \leq 1$, both conditions are satisfied when

$$\tau\Sigma_{T,1\to2}\phi_1^0 \ll 1.$$ (15)

In the following, we examine the conditions under which (15) is satisfied. We can use the steady–state version of equation (4) to study the saturation phenomenon exactly. In steady state we obtain

$$0 = -\Sigma_{T,1\to2}\overline{\phi}_1 N_g + \frac{1}{\tau}(N_0 - N_g),$$

or

$$N_g = \frac{N_0}{1 + \tau \Sigma_{T,1\to2}\phi_1^0},$$ (16)

whose Fourier transform is well approximated by equation (13) when $\tau \Sigma_{T,1\to2}\phi_1^0 \ll 1$. Figure 1 shows saturation curves for different mean lifetimes and excitation intensities.

If we choose arbitrarily not to permit more than 1% fluorophore saturation, then the maximum allowable excitation is

$$\phi_1^0 = \frac{1}{99\tau\Sigma_{T,1\to2}}.$$ (17)

Table 1 lists the maximum acceptable excitation intensities under this criterion for different combinations of mean lifetime and microscopic cross section. The fluorophore molar extinction coefficient $\varepsilon \left[cm^{-1}M^{-1}\right]$ and $\Sigma_{T,1\to2}$ are related by:

$$\varepsilon = \frac{A_0\Sigma_{T,1\to2}}{1000\ln10},$$ (18)

where A_0 is Avogadro's number, 6.022×10^{23} mol^{-1}.

4. Sensitivity Study for a Modulated Waveform

Computation of the Forward Problem

There are two necessary conditions for successful detection of mean lifetime perturbations by means of a fluorescence measurement. The first is that the perturbation produce an appreciable change in some property of the emissive source (*e.g.*, DC intensity, AC amplitude, or AC phase). The second is that the change so produced have an appreciable impact on one or more detector readings. The emissive source is a function of the concentration, extinction coefficient, mean lifetime and quantum yield of the fluorophore, and of the excitation intensity. The background medium is not itself affected by the fluorophores but behaves like a filter that modifies the excitation and emission fields by scattering and absorption.

Below, we list the expressions used in the computation of expected detector responses for a time–harmonic source, given the optical properties of the background medium, fluorophore concentration, lifetime and quantum yield. The source term for the fluorescence light is

$$s_2 = \frac{\gamma\widetilde{N}_s}{4\pi\tau} = \frac{\gamma\Sigma_{T,1\to2}N_0\widetilde{\overline{\phi}}_1}{4\pi(1+j\omega\tau)} = \frac{\gamma\Sigma_{T,1\to2}N_0\widetilde{\overline{\phi}}_1}{\sqrt{1+\omega^2\tau^2}}e^{-j\tan^{-1}\omega\tau} = \frac{\Sigma_{T,1\to2}N_0\widetilde{\overline{\phi}}_1}{\tau_0\sqrt{\frac{1}{\tau^2}+\omega^2}}e^{-j\tan^{-1}\omega\tau}.$$ (19)

Let τ_0 be fixed while τ varies because of the change of the nonradiative de–excitation rates of the excited fluorophores. When $\omega\tau \ll 1$,

$$s_2 \approx \frac{\tau}{\tau_0}\Sigma_{T,1\to2}N_0\widetilde{\overline{\phi}}_1e^{-j\omega\tau},$$ (20)
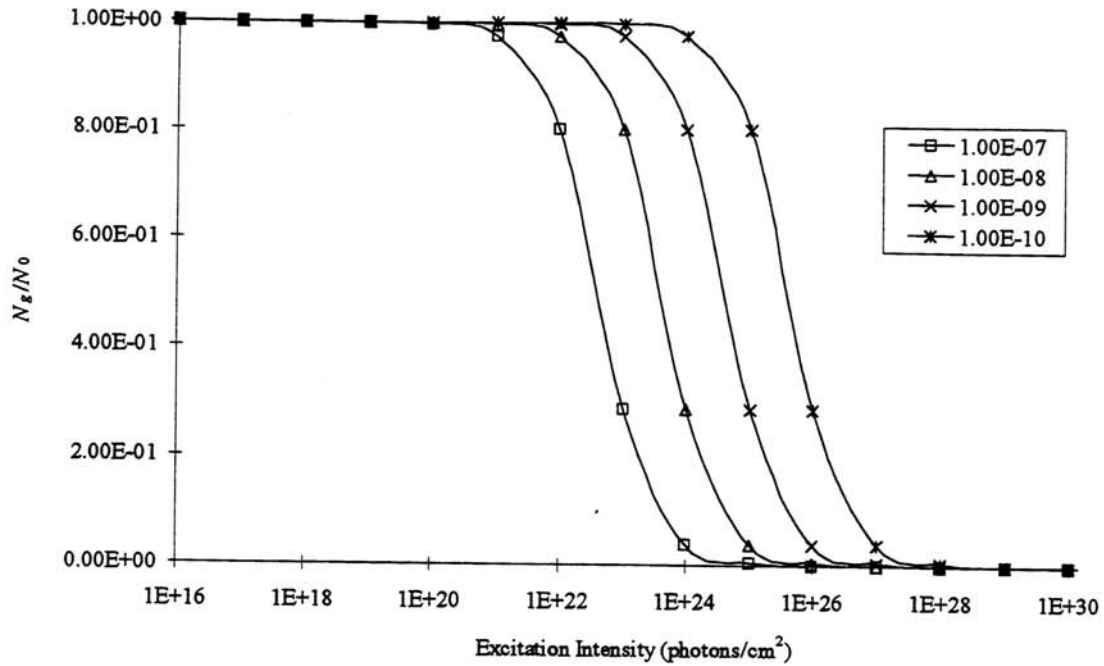
Figure 1. Fluorophore saturation as a function of excitation intensity for different mean lifetimes, and assuming a fluorophore molar extinction coefficient of $3.47 \times 10^5 \ cm^{-1}M^{-1}$.

$\tau[s]$	$\Sigma_{T,1\to2} \ [cm^2]$					
	1.00E-15	2.50E-16	6.25E-17	1.56E-17	3.91E-18	9.77E-19
	$\varepsilon [cm^{-1}M^{-1}]$					
	1.39E+06	3.47E+05	8.66E+04	2.17E+04	5.41E+03	1.35E+03
1.00E+00	1.01E+13	4.04E+13	1.62E+14	6.46E+14	2.59E+15	1.03E+16
1.00E-01	1.01E+14	4.04E+14	1.62E+15	6.46E+15	2.59E+16	1.03E+17
1.00E-02	1.01E+15	4.04E+15	1.62E+16	6.46E+16	2.59E+17	1.03E+18
1.00E-03	1.01E+16	4.04E+16	1.62E+17	6.46E+17	2.59E+18	1.03E+19
1.00E-04	1.01E+17	4.04E+17	1.62E+18	6.46E+18	2.59E+19	1.03E+20
1.00E-05	1.01E+18	4.04E+18	1.62E+19	6.46E+19	2.59E+20	1.03E+21
1.00E-06	1.01E+19	4.04E+19	1.62E+20	6.46E+20	2.59E+21	1.03E+22
1.00E-07	1.01E+20	4.04E+20	1.62E+21	6.46E+21	2.59E+22	1.03E+23
1.00E-08	1.01E+21	4.04E+21	1.62E+22	6.46E+22	2.59E+23	1.03E+24
1.00E-09	1.01E+22	4.04E+22	1.62E+23	6.46E+23	2.59E+24	1.03E+25
1.00E-10	1.01E+23	4.04E+23	1.62E+24	6.46E+24	2.59E+25	1.03E+26
1.00E-11	1.01E+24	4.04E+24	1.62E+25	6.46E+25	2.59E+26	1.03E+27
1.00E-12	1.01E+25	4.04E+25	1.62E+26	6.46E+26	2.59E+27	1.03E+28

Table 1. List of the maximum acceptable excitation intensity, ϕ_1^0, for indicated mean lifetimes and microscopic cross sections.

and when $\omega\tau \gg 1$,

$$s_2 \approx \frac{\gamma\Sigma_{T,1\rightarrow2}N_0\widetilde{\widetilde{\phi}}_1}{\omega\tau}e^{-j\frac{\pi}{2}} = -j\frac{\Sigma_{T,1\rightarrow2}N_0\widetilde{\widetilde{\phi}}_1}{\omega\tau_0}. \tag{21}$$

Figure 2 demonstrates the amplitude and phase of s_2 as a function of τ. Inspection of Figure 2 and equations (20) and (21) reveals that when τ_0 is fixed, the source term for fluorescence emission is sensitive to changes in τ or in $\omega\tau$ when $\omega\tau \ll 1$, and is insensitive to either of them when $\omega\tau \gg 1$. Figure 3 demonstrates the frequency responses of amplitude and phase of the emissive source s_2, for three different mean lifetimes, assuming an intrinsic mean lifetime of 10^{-8} s. The sensitivity of the response at a fixed frequency can be decided by the separations between these three curves. Inspection of Figure 3 indicates that maximum sensitivity occurs at DC for amplitude data, and in the 50–200 MHz range for phase data.
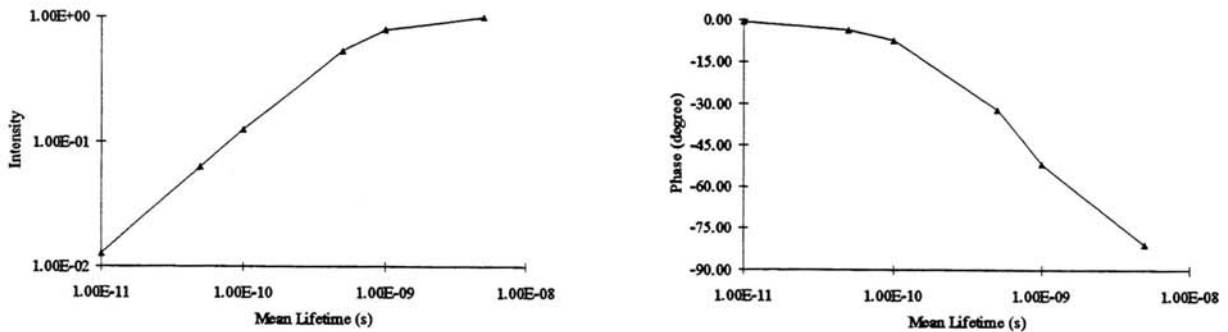

Figure 2. Amplitude (normalized) and phase of the emission intensity source as a function of mean lifetime (s) for 200 MHz modulation frequency. Assumes that $\tau_0 = 5\times10^{-9}$ s, $\widetilde{\widetilde{\phi}} = 10^{18}$ cm^{-2}, $\varepsilon = 2\times10^5$ cm^{-1}M^{-1}, and $N_0 = 6\times10^{13}$ cm^{-3}.
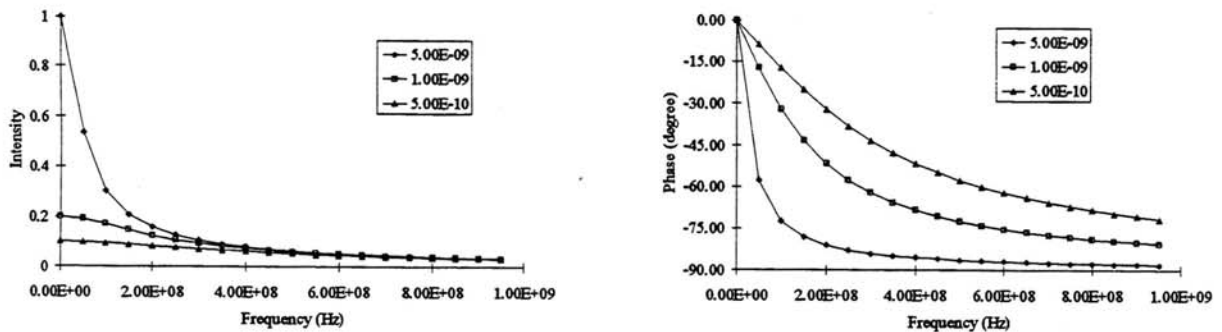

Figure 3. Amplitude and phase of the emission source intensity as a function of mean lifetime and modulation frequency. Assumes that $\tau_0 = 5\times10^{-9}$ s, $\widetilde{\widetilde{\phi}} = 10^{18}$ cm^{-2}, $\varepsilon = 2\times10^5$ cm^{-1}M^{-1}, and $N_0 = 6\times10^{13}$ cm^{-3}.

Demodulation

Another factor that must be considered in assessing sensitivity is the demodulation of the emissive source. If we assume that the excitation field modulation is 100%, then the emissive source modulation is:

$$M = \frac{s_2(\omega)}{s_2(0)} = \frac{\sqrt{\frac{1}{\tau^2}}}{\sqrt{\frac{1}{\tau^2} + \omega^2}} = \frac{1}{\sqrt{1 + \tau^2\omega^2}}. \tag{22}$$

Thus, to achieve a high modulation, both the mean lifetime and the modulation frequency should be as low as possible. A rule of thumb can be derived for a given dynamic range of mean lifetime. If we choose 10% as an acceptable threshold for modulation, then

$$\frac{1}{\sqrt{1 + \tau^2\omega^2}} = \frac{1}{\sqrt{1 + (2\pi f\tau)^2}} \geq 0.1 \qquad \Rightarrow \qquad f \leq \frac{\sqrt{99}}{2\pi\tau} \approx \frac{1.584}{\tau}.$$

Table 2 illustrates the maximum modulation frequency that can be used for different mean lifetimes, assuming 10% is the minimum acceptable modulation.

τ	1.00E-10	5.00E-10	1.00E-09	5.00E-09	1.00E-08
f	1.58E+10	3.17E+09	1.58E+09	3.17E+08	1.58E+08

Table 2. List of permissible maximum frequency for a given mean lifetime assuming a 10% modulation threshold.

5. Experiments and Image Reconstruction

Experimental Setup

Figure 4 shows the experimental tissue phantoms and Figure 5 illustrates the source and detector configurations. Two experiments were performed, one with two balloons and no added dye in the background, the other with a single balloon but with a low concentration of dye added to the background. In both experiments, a 0.75W, multi-line (average wavelength ~490 μm) argon laser source was used to irradiate the phantom. A filter blocked excitation light from entering the detector. The detector was a Hamamatsu C3140 CCD camera directed normal to the phantom to collect the emission light. In the first experiment, a limited illumination angle was used. The detectors were located at every 30° along the border of the cylinder and the source was positioned every 10° from 90° to 150° counterclockwise relative to the source. In the second experiment, the sources were rotated every 30° around the boundary of the phantom, and the detectors were positioned every 30° from 90° to 270° clockwise relative to each source location. Dark current was measured before the experiment. The source intensity was recorded for each measurement using a Coherent Labmaster-E. Each measurement was then corrected for the dark current, source intensity, and lens aperture. At least two measurements were taken and averaged to obtain the detector readings for each source-detector pair. In the first experiment, balloons containing different volumes (0.8 and 1.2 mL) of Rhodamine 6G dye at a concentration of ~50 μM were embedded in a 8 cm diameter cylindrical phantom filled with 0.2% Intralipid® (% lipid per unit volume). The same cylindrical phantom was used in the second experiment except the Intralipid concentration was 0.33% and contained 0.1 μM dye. The volume of the balloon was 0.5 mL, and contained 100 μM dye.

The optical thickness of the phantom medium was ~20 and ~33 transport mean free pathlengths, respectively, for the excitation and emission light. Weight functions for the corresponding reference media were computed by Monte Carlo simulation assuming a optical thickness of 20 transport mean free paths.

Image Reconstruction

Image reconstructions were performed using three iterative algorithms — POCS, CGD, and SART — with a rescaling technique and positivity constraints [4]. Three types of 2-D reconstruction were performed, as shown in Figure 6. The Type-1 reconstruction of Figure 6A assumed symmetry along the *z*-axis and the weight function of voxels with the same *z*-coordinate were summed up to obtain an integrated value. The Type-2 reconstruction of Figure 6B assumed that only
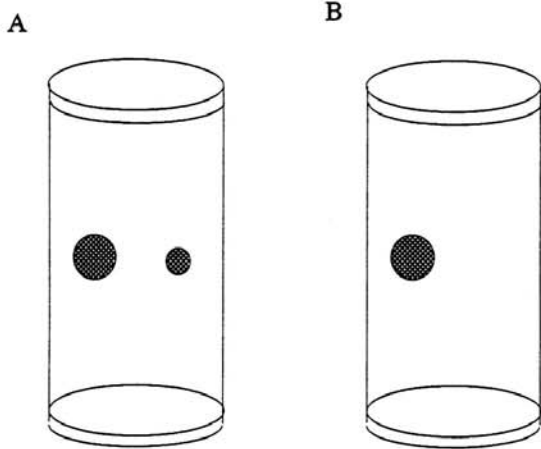
Figure 4. (A) Tissue phantom for the first experiment, where two balloons were suspended in the cylinder; (B) phantom for the second experiment, where only one balloon was used.
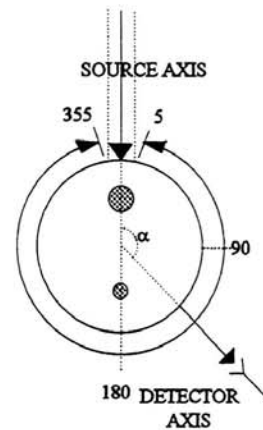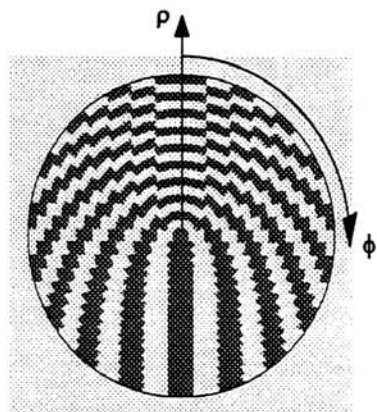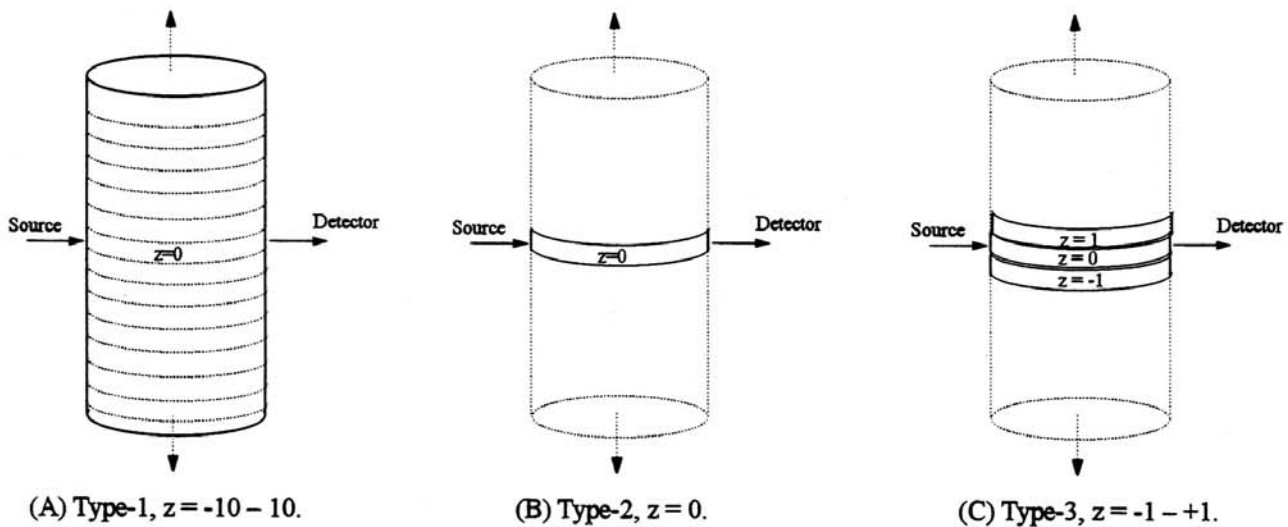
Figure 5. Source and detector configurations.

(A) Type-1, z = -10 – 10.

(B) Type-2, z = 0.

(C) Type-3, z = -1 – +1.

(D) Cylindrical Coordinate System

Figure 6. Three reconstruction types – (A) Type-1 reconstruction where axial symmetry was assumed along the z-axis, (B) Type-2 reconstruction where it is assumed that fluorophore is present only in plane $z = 0$, and (C) Type-3 reconstruction where it is assumed that fluorophore is present only in plane $z = -1$, 0, or 1. The cylindrical coordinate system used to digitize the phantom is shown in (D).

voxels on the $z = 0$ plane contain fluorescent dye, and only voxels on that plane were considered for reconstruction. The Type-3 reconstruction of Figure 6C assumed that only voxels in the $z = -1$, 0, or 1 plane contain fluorescent dye and that its concentration along the z-axis is constant. In this case, the weight function for voxels in these three planes with the same z-coordinate were summed to yield an integrated value. Only the central plane of the reconstruction results are displayed. Figure 4D demonstrates the cylindrical coordinate system, where the ρ- and ϕ- coordinates are shown in the figure and the z-coordinate is normal to the paper. There are 400 voxels in each plane. Only Type-1 reconstruction was performed for the first experiment, while all three types of reconstruction were performed for the second experiment.

Results

Figure 7 shows the type-1 reconstruction results from the first experiment using the CGD method after 10, 100, 1000, and 10,000 iterations. The two balloons are located, and artifacts are observed on the boundary. The two inhomogeneities are about the same size but with different intensities, which roughly coincides with the difference in balloon volume. The image quality improves as the number of iterations increases. Figure 8 illustrates the comparison of the type-1 reconstruction results of the three algorithms after 10 and 1,000 iterations. Results of all three algorithms show fuzzy images early in the reconstruction, but distinguishable inhomogeneities are observable for the POCS and CGD algorithms. After 1,000 iterations, all three algorithms are able to resolve two inhomogeneities with artifacts. Figure 9 shows reconstruction results from the second experiment using the CGD method for the three reconstruction types after 10, 100, 1,000, and 10,000 iterations. All three types reasonably locate the position of the balloon, while artifacts are observed on the boundary of the cylinder. No significant difference is observed between the type-2 and type-3 reconstructions.

6. Discussion and Conclusions

In this study, two coupled transport equations, (2) and (6), were used to describe the migration of the excitation and emitted fluorescent light. The equations for excitation and emission intensities are related by the dynamic equation, (4), for the fluorophore concentrations in the ground and excited states. The solution to Equation 4, which is essentially the source term for fluorescence, is a constant for DC excitation. However, for a time-harmonic excitation, the solution yields a combination of the fundamental frequency and higher order harmonics. If most of the fluorophores are in the ground state, the amplitudes of the higher order harmonics are small and they can be safely ignored (see Table 1, Figure 1).

The ability to measure a modulated waveform depends on the optical properties of the background medium and of the fluorescence source because both act to damp the propagating fluorescence signal. The latter, in turn, is a function of the fluorophore concentration, quantum yield and mean lifetime, and the excitation intensity. In this paper, we presented results of a study on the effects of varying the modulation frequency and fluorophore mean lifetime. From the mean lifetime sensitivity study, we conclude that for a fixed intrinsic lifetime, τ_0, the fluorescence source strength is sensitive to the product of mean lifetime and modulation frequency, $\omega\tau$, when $\omega\tau \ll 1$, and is insensitive to it when $\omega\tau \gg 1$. The frequency sensitivity study demonstrates that the intensity and phase of the fluorescence source are most sensitive at low (DC) and intermediate (50–200 MHz) modulation frequencies, respectively. Thus, to obtain optimal sensitivity, short mean lifetime fluorophores and intermediate modulation frequencies should be used. If a long lifetime fluorophore is used, a low modulation frequency should be used, and only the intensity need be measured since the phase is not sensitive to changes in mean lifetime in this case. The demodulation caused by the fluorophore has a direct impact on the measured AC intensity, although it does not change the relative sensitivity. Thus, even though demodulation does not influence the relative sensitivity, as a practical matter, demodulation may attenuate the AC signal to an unmeasurable level. Our results show that demodulation of the fluorescence source is inversely proportional to the mean lifetime and frequency. This poses another limit to the use of long lifetime fluorophores and higher modulation frequencies.

Imaging operators were derived in this study for DC (11) and time-harmonic (12) sources. The operator for the DC source can reconstruct the product of quantum yield and fluorophore concentration, γN_0, while the operator for the AC source can reconstruct the mean lifetime once γN_0 is known. The quantum yield and fluorophore concentration are not separable because they both contribute to the AC and DC fluorescent source intensity. The mean lifetime, on the other hand, influences only the AC fluorescent source.

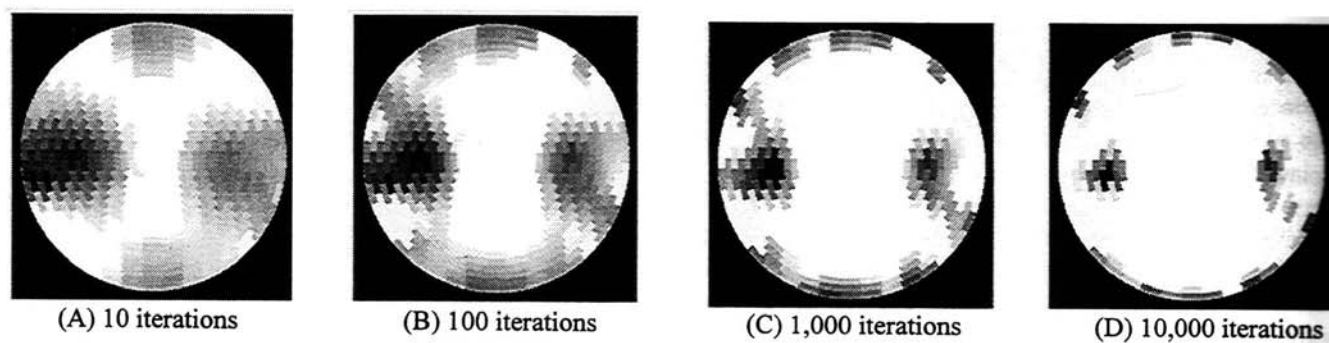(A) 10 iterations   (B) 100 iterations   (C) 1,000 iterations   (D) 10,000 iterations

(E) Target

Figure 7. Type-1 reconstruction results from the first experiment using CGD method after (A) 10 iterations, (B) 100 iterations, (C) 1,000 iterations, and (D) 10,000 iterations. The target is shown in (E).
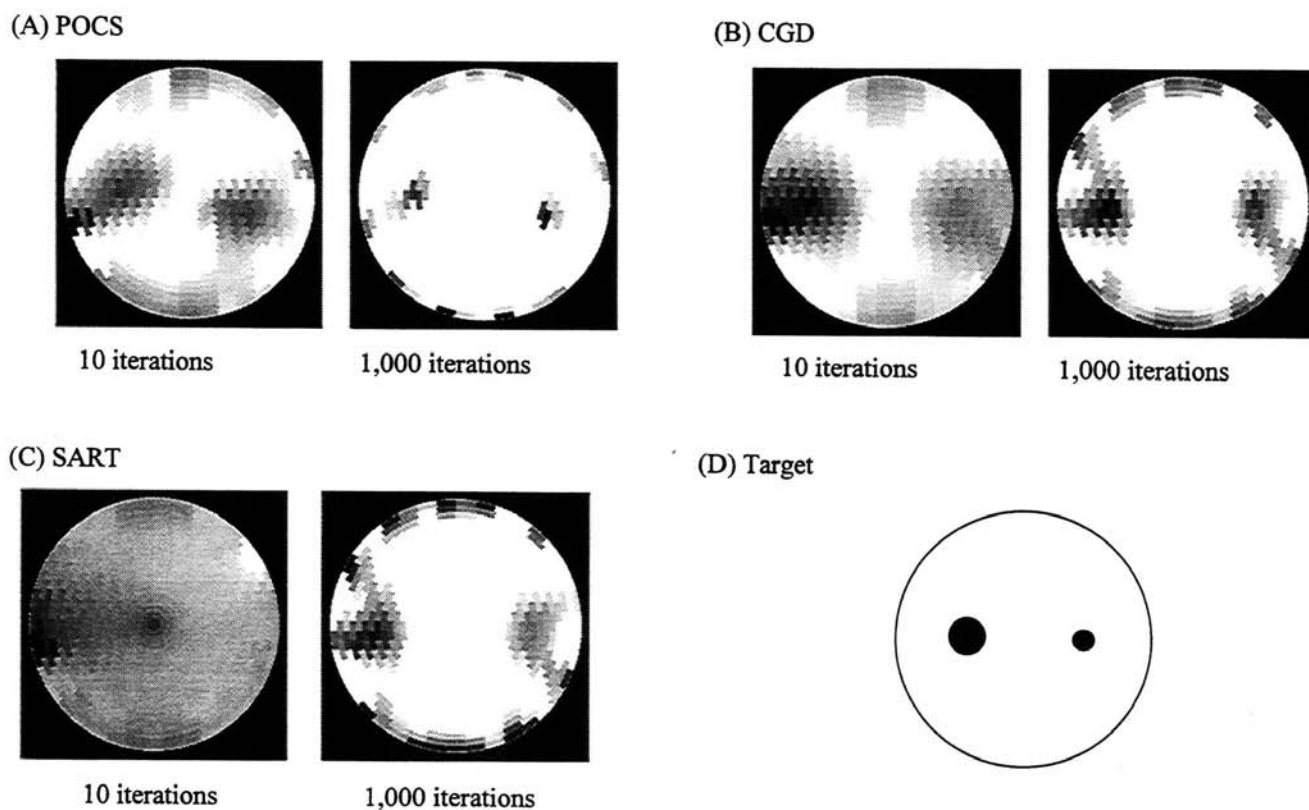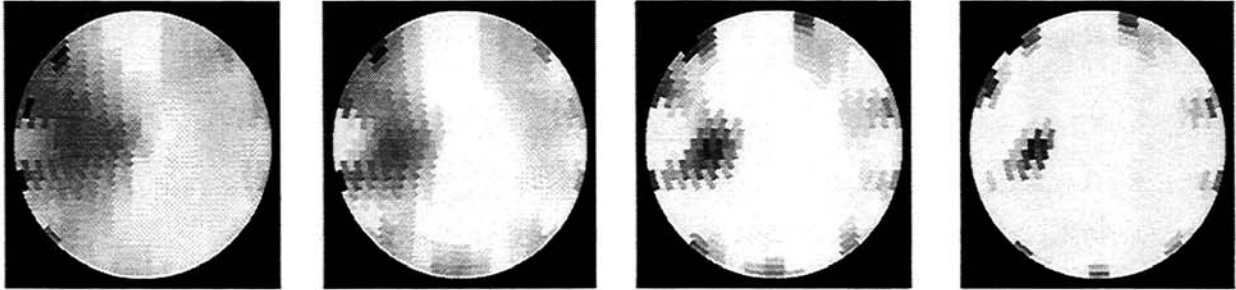
(A) POCS

10 iterations   1,000 iterations

(B) CGD

10 iterations   1,000 iterations

(C) SART

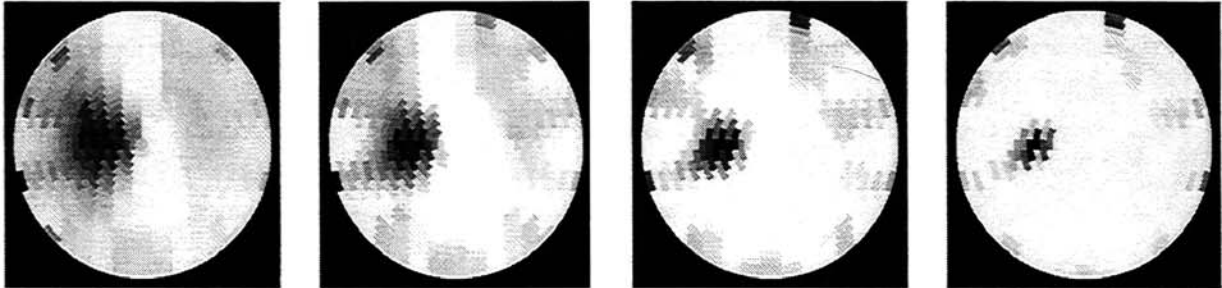10 iterations   1,000 iterations

(D) Target

Figure 8. Type-1 reconstruction results from the first experiment using (A) POCS, (B) CGD, and (C) SART algorithms after 10 and 1,000 iterations. (D) is the target.
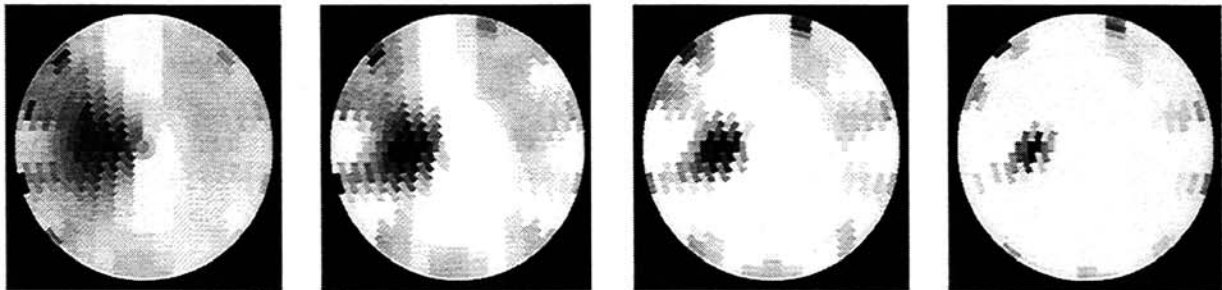
(A) Type-1

(B) Type-2

(C) Type-3

| 10 | 100 | 1,000 | 10,000 |

Figure 9. Reconstructed images, from the second set of experimental data using the CGD algorithm and all three reconstruction types after 10, 100, 1,000, and 10,000 iterations.

Reconstructions of experimental data were conducted using limited angle views obtained from simply structured phantom media. These experiments are meant to represent a crude model of tissue containing fluorophores that have been selectively bound to a pathology having defined specificity that can be recognized by an antibody or other biomolecule. In both cases, the location of the balloons were correctly identified, qualitatively, with artifacts present at the boundary. The relatively enhancement in contrast effected by the presence of a fluorophore will depend strongly on the ratio of the concentration of fluorophore bound to a specified target to that in the background. We recognize that the conditions examined here are highly idealized and the target-to-background ratio of fluorophore in a real tissue would be much lower. Nevertheless, the results obtained from the single fluorophore experiment are encouraging.

Comparison of the different reconstruction conditions examined show that the quality of the type-1 reconstruction results is somewhat poorer than those of the other reconstruction types. This is not unexpected, because the type-2 and type-3 reconstructions more closely approximate the real experimental setup, while type-1 reconstruction introduces a systematic error by assuming symmetry along the z-axis. The image quality, however, is degraded by only a small amount.

7. Acknowledgment

8. References

1. A. V. Kak and M. Slaney, *Principles of Computerized Tomographic Imaging.* IEEE Press, New York, NY, 1988.

2. *Image Recovery: Theory and Application,* H. Stark, ed., Academic Press, New York, NY, 1987.

3. J. R. Lakowicz, *Principles of Fluorescence Spectroscopy,* Plenum Press, New York,, 1983.

4. *Medical Optical Tomography: Functional Imaging and Monitoring,* G. Müller *et al.*, eds., SPIE Institutes vol. IS11, SPIE Press, Bellingham, WA, 1993.

5. *OSA Proceedings on Advances in Optical Imaging and Photon Migration,* R. R. Alfano, ed., vol. 21, Optical Society of America, Washington, DC, 1994.

6. D. C. Youla, "Mathematical Theory of Image Reconstruction," *Image Recovery: Theory and Application,* Henry Stark, ed., New York: Academic Press, 1987.

7. P. E. Gill, W. Murray, M. H. Wright, *Practical Optimization,* New York: Academic Press, 1981.

8. NCRP Scientific Committee 52, *Conceptual Basis for Calculations of Absorbed–Dose Distribution,* NCRP Report No. 108, 1991.

9. J. Chang, R. Aronson, H. L. Graber, R. L. Barbour "Imaging diffusive media using time-independent and time-harmonic sources: dependence of image quality on imaging algorithms, target volume, weight matrix, and view angles," in *Proc. Optical Tomography, Photon Migration, and Spectroscopy of Tissue and Model Media: Theory, Human Studies, and Instrumentation,* vol. SPIE-2389, (San Jose), Feb. 1995.

10. J. Chang, H. L. Graber, R. L. Barbour, "Image reconstruction of dense scattering media from CW sources using constrained CGD and a matrix rescaling technique," in *Proc. Optical Tomography, Photon Migration, and Spectroscopy of Tissue and Model Media: Theory, Human Studies, and Instrumentation,* vol. SPIE-2389, (San Jose), Feb. 1995.